Molecular basis for lipid recognition by the prostaglandin D_2 receptor CRTH2

Heng Liu[a,1], R. N. V. Krishna Deepak[b,1], Anna Shiriaeva[c,d,1], Cornelius Gati[c,e], Alexander Batyuk[f], Hao Hu[g], Uwe Weierstall[g], Wei Liu[h,i], Lei Wang[a], Vadim Cherezov[c,d,e,2], Hao Fan[b,2], and Cheng Zhang[a,2]

[a]Department of Pharmacology and Chemical Biology, School of Medicine, University of Pittsburgh, Pittsburgh, PA 15261; [b]Bioinformatics Institute, Agency for Science, Technology and Research, Matrix 138671, Singapore; [c]Bridge Institute, University of Southern California Michelson Center for Convergent Biosciences, University of Southern California, Los Angeles, CA 90089; [d]Department of Chemistry, University of Southern California, Los Angeles, CA 90089; [e]Department of Biological Sciences, University of Southern California, Los Angeles, CA 90089; [f]Linac Coherent Light Source, Stanford Linear Accelerator Center National Accelerator Laboratory, Menlo Park, CA 94025; [g]Department of Physics, Arizona State University, Tempe, AZ 85281; [h]Center for Applied Structural Discovery at the Biodesign Institute, Arizona State University, Tempe, AZ 85281; and [i]School of Molecular Sciences, Arizona State University, Tempe, AZ 85281

Edited by Robert J. Lefkowitz, HHMI, Durham, NC, and approved June 21, 2021 (received for review February 10, 2021)

Prostaglandin D_2 (PGD_2) signals through the G protein–coupled receptor (GPCR) CRTH2 to mediate various inflammatory responses. CRTH2 is the only member of the prostanoid receptor family that is phylogenetically distant from others, implying a nonconserved mechanism of lipid action on CRTH2. Here, we report a crystal structure of human CRTH2 bound to a PGD_2 derivative, 15R-methyl-PGD_2 (15mPGD$_2$), by serial femtosecond crystallography. The structure revealed a "polar group in"–binding mode of 15mPGD$_2$ contrasting the "polar group out"–binding mode of PGE_2 in its receptor EP3. Structural comparison analysis suggested that these two lipid-binding modes, associated with distinct charge distributions of ligand-binding pockets, may apply to other lipid GPCRs. Molecular dynamics simulations together with mutagenesis studies also identified charged residues at the ligand entry port that function to capture lipid ligands of CRTH2 from the lipid bilayer. Together, our studies suggest critical roles of charge environment in lipid recognition by GPCRs.

CRTH2 (DP2) | prostaglandin D_2 | lipid binding | crystal structure | MD simulations

Eicosanoids constitute a group of signaling lipid mediators that are derived from arachidonic acid or other polyunsaturated fatty acids (1, 2). As the name indicates, they all possess a long hydrocarbon chain with 20 carbon units, which is usually attached to a carboxylic acid head group. Prostanoids including prostaglandins D_2, E_2, and F_2 (PGD_2, PGE_2, and PGF_2); prostacyclin (PGI_2); thromboxane A_2 (TXA_2) and leukotrienes including leukotriene B_4, C_4, and D_4 (LTB_4, LTC_4, and LTD_4) are representative endogenous eicosanoids that can induce signaling through G protein–coupled receptors (GPCRs) to play critical roles in inflammation, immunity, hemostasis, and tissue repair (1, 3–5). In humans, nine prostanoid receptors have been identified: PGD_2 receptors 1 and 2 (DP1 and DP2), PGE_2 receptors 1 to 4 (EP1 to EP4), PGF_2 receptor (FP), PGI_2 receptor (IP), and TXA_2 receptor (TP) (5). All of these receptors, except for DP2, belong to the α-branch of Class A GPCRs as close phylogenetic neighbors of aminergic receptors (5, 6). DP2, chemoattractant receptor–homologous molecule expressed on type 2 helper T cells (Th2) (also named CRTH2), is more closely related to a group of chemotactic GPCRs in the γ-branch of Class A GPCRs, including chemokine receptors and receptors for LTB_4, formylpeptides, and complement peptides C3a and C5a (6, 7).

Certain types of immune cells, including eosinophils, innate lymphoid cells, and Th2 cells, express high levels of CRTH2 (8–11). PGD_2 signaling through CRTH2 can induce chemotaxis of these immune cells, which is a major pathway that drives the onset of type 2 inflammation (11–15). Therefore, the roles of PGD_2–CRTH2 signaling axis in type 2 inflammation-related diseases such as asthma and allergic rhinitis have attracted outstanding research interest (14, 16, 17). CRTH2 antagonists hold the potential of being a new class of anti-inflammatory drugs (16, 18–24). Although clinical trials have generated mixed results on different CRTH2 antagonists for asthma (17–20, 25), it is likely that a certain subpopulation of patients, such as those with a high baseline of Th2 cells or eosinophils, may benefit most from anti-CRTH2 therapy (17, 24). In addition, it has been proposed that insurmountable CRTH2 antagonists with prolonged receptor residence time can provide better, therapeutic efficacy, compared to reversible and fast, dissociating CRTH2 antagonists, which needs further investigation (26).

We have previously reported crystal structures of CRTH2 bound to two antagonists, CAY10471 and fevipiprant, which revealed a positively charged environment of the ligand-binding pocket and a potential ligand entry port (27). The structural analysis of antagonist-bound CRTH2 suggested that PGD_2 may enter the ligand-binding pocket through the ligand entry port by opposite charge attraction (27). Recently, crystal structures of several other prostanoid receptors, EP3, EP4, and TP, and cryogenic electron microscopy (cryo-EM) structures of the EP2 and EP4 signaling complexes with PGE_2 have also been reported (28–33). To further study the binding of lipid agonists to CRTH2 and investigate if CRTH2 differs from other prostanoid receptors in lipid recognition and receptor activation, we determined a 2.6-Å resolution, room temperature crystal

Significance

Many amphipathic lipids, including cannabinoids, lysophospholipids, prostanoids, and leukotrienes, bind to G protein–coupled receptors (GPCRs) through the lipid bilayer. How these lipid ligands get anchored to their receptors and enter ligand-binding pockets is largely elusive. Our results revealed a distinctive lipid recognition mechanism for the prostaglandin D_2 (PGD_2) receptor CRTH2 that is not shared by other prostanoid receptors. Based on the structural analysis, we propose two representative binding modes of lipids in GPCRs. We also identified critical structural motifs and conformational changes of CRTH2 for capturing lipids from the lipidic environment and lipid transition to the binding pocket, thereby offering unprecedented molecular insight into the dynamic lipid-binding processes for GPCRs.

Author contributions: H.L., R.N.V.K.D., V.C., H.F., and C.Z. designed research; H.L., R.N.V.K.D., A.S., C.G., A.B., H.H., U.W., W.L., L.W., V.C., H.F., and C.Z. performed research; H.L., R.N.V.K.D., A.S., C.G., A.B., H.H., U.W., W.L., V.C., H.F., and C.Z. analyzed data; and H.L., R.N.V.K.D., V.C., H.F., and C.Z. wrote the paper.

The authors declare no competing interest.

This article is a PNAS Direct Submission.

[1]H.L., R.N.V.K.D., and A.S. contributed equally to this work.

[2]To whom correspondence may be addressed. Email: chengzh@pitt.edu, fanh@bii.a-star.edu.sg, or cherezov@usc.edu.

This article contains supporting information online at https://www.pnas.org/lookup/suppl/doi:10.1073/pnas.2102813118/-/DCSupplemental.

Published August 2, 2021.

structure of CRTH2 bound to a PGD_2 derivative by serial femtosecond crystallography (SFX) using an X-ray free electron laser (XFEL) source. We performed computational simulation studies using the CRTH2–15R-methyl-PGD_2 ($15mPGD_2$) structure, which helped identify the roles of specific residues surrounding the ligand entry port and provided molecular insights into the events that could facilitate ligand binding. Results from our mutational analysis of the identified residues helped us further strengthen the proposed model for ligand capture and entry in CRTH2.

Results

Structure Determination of Lipid Agonist-Bound CRTH2 by Serial Femtosecond Crystallography. We used the same construct of human CRTH2 that we previously used to solve crystal structures of antagonist-bound CRTH2 (27). To facilitate crystallogenesis, an engineered T4 lysozyme (mT4L) with an additional eight-residue linker was inserted into the intracellular loop 3, flexible C terminus was truncated at R340, and the potential glycosylation site N25 was mutated to alanine. The crystallization construct showed a comparable PGD_2-binding ability as the wild-type CRTH2 (wtCRTH2) (27). We used $15mPGD_2$ instead of PGD_2 in our structural studies because $15mPGD_2$ has a higher affinity for CRTH2 (*SI Appendix*, Fig. S1*A*), and it is a selective prostaglandin agonist for CRTH2 over the DP1 (34). The only difference between $15mPGD_2$ and PGD_2 is a methyl group at the 15-position carbon (C-15) (Fig. 1*A*). The crystals of CRTH2 bound to $15mPGD_2$ were obtained in the lipidic cubic phase (LCP) (35). Because of the small sizes of crystals (maximal crystal size <10 μm), we used XFEL to collect SFX data and solved the crystal structure at an anisotropic resolution of 2.6 to 3.2 Å (*Materials and Methods*) (*SI Appendix*, Fig. S1*B* and Table 1). We observed clear and strong electron density of the ligand. Our calculated simulated-annealing ligand-omit map was continuous, even when contoured at 4 σ, which allowed unambiguous modeling of $15mPGD_2$ in the structure (*SI Appendix*, Fig. S1*C*).

Overall Structure and Lipid-Binding Mode. The overall structure of $15mPGD_2$-bound CRTH2 is nearly identical to the antagonist fevipiprant-bound CRTH2 (27), with a rmsd of 0.39 Å for all atoms of CRTH2 in both structures (Fig. 1*B*), suggesting that we captured an agonist-bound, inactive conformation of the receptor. Specifically, important structural motifs for receptor activation can be well aligned in both structures (*SI Appendix*, Fig. S1*D*). It is likely that agonists alone cannot stabilize CRTH2 in an active conformation, similarly to that observed for the β_2-adrenergic receptor (36) and melatonin receptors (37, 38). Additionally, the inactive receptor conformation may be constrained by the fusion partner.

The lipid agonist $15mPGD_2$ occupies the same ligand-binding pocket in CRTH2 as the antagonist fevipiprant (Fig. 1*C*). The N-terminal region of CRTH2 bound to $15mPGD_2$ forms a well-folded structure with an α-helix (N-helix) and a loop (N-loop). The gap formed between the N-loop and the extracellular part of TM7 has been proposed to serve as the potential ligand entry port (27). The N-helix and the extracellular loop 2 (ECL2) constitute a lid domain to cover the binding pocket for $15mPGD_2$, leaving the ligand entry port as the only open end of the ligand-binding pocket (Fig. 1*D*). $15mPGD_2$ adopts a "U" shape–binding pose with the two hydrocarbon chains extending from the central hydroxycyclopentanone ring almost parallel to each other. The carboxyl head group of $15mPGD_2$ can be well superimposed to the carboxyl group of fevipiprant, which forms a similar polar interaction network with nearby residues $R170^{ECL2}$, $Y184^{ECL2}$, $K210^{5.42}$, and $Y262^{6.51}$ [superscripts indicate Ballesteros–Weinstein numbering (39)] (Fig. 1*E*). The alkyl ω-chain of $15mPGD_2$ is surrounded by mostly aromatic residues, including $F87^{2.60}$, $F90^{2.63}$, $W97^{ECL1}$, $H107^{3.28}$, $F111^{3.32}$, $Y183^{ECL2}$, and $F294^{7.43}$. These residues together with $P287^{7.36}$ and $L286^{7.35}$ form extensive

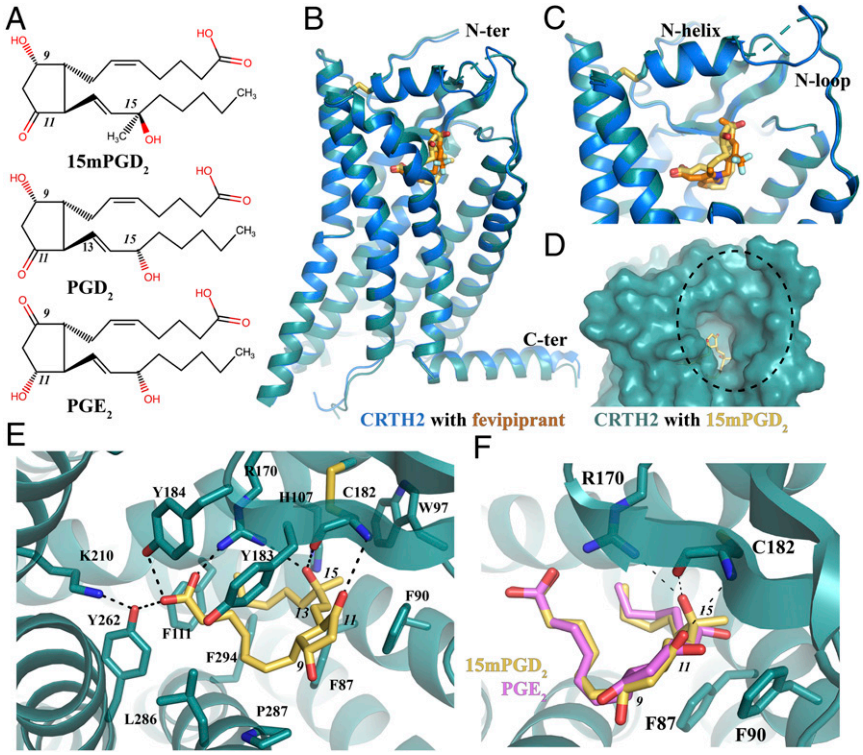

Fig. 1. Overall structure of CRTH2 bound to $15mPGD_2$ and its ligand-binding pocket. (*A*) Chemical structures of $15mPGD_2$, PGD_2, and PGE_2. C-9, C-11, and C-15 positions are indicated with italic numbers. (*B*) Overall structure of CRTH2 bound to $15mPGD_2$ and structure alignment with CRTH2 bound to fevipiprant. (*C*) Overlapping, binding positions of $15mPGD_2$ and fevipiprant. (*D*) Potential lipid entry port. (*E*) Binding pocket of $15mPGD_2$. (*F*) Docking of PGE_2 (pink) into the $15mPGD_2$- (yellow) binding pocket. Hydrogen bonds are shown as dashed lines.

Table 1. Data collection and refinement statistics of CRTH2–15mPGD2 complex

Number of crystals	7,061
Space group	$P2_12_12_1$
Cell dimensions, Å	
a	51.4
b	67.8
c	265.4
Resolution, Å	32.4–2.60 (2.69–2.60)*
No. reflections	1,809,804 (12,462)
No. unique reflections	29,269 (2,540)
Rsplit, %	26.4 (513.5)
Mean I/σ(I)	2.4 (0.2)
CC*, %	99.1 (51.2)
Completeness, %	98.9 (90.6)
Multiplicity	61.8 (4.9)
Refinement	
Resolution, Å	32.4–2.6†
No. reflections/free set	15,632/781
Rwork/Rfree	0.229/0.267
No. atoms	
Protein	3,424
Ligand	26
Water and ions	51
B-factors, $Å^2$	
Overall	52.3
Protein	52.1
Ligand	36.2
Water and ions	77.2
rmsds	
Bond lengths, Å	0.002
Bond angle, °	0.48
Ramachandran stats, %	
Favored	95.12
Allowed	4.88
Disallowed	0

*Values in parentheses are for highest-resolution shell.
†Data were anisotropically truncated by the STARANISO web server at 3.2-, 3.2-, and 2.6-Å resolution along the reciprocal unit cell vectors a*, b*, and c*, respectively.

hydrophobic interactions with the ω-chain of $15mPGD_2$ (Fig. 1*E*). Supporting such a binding mode, previous mutagenesis studies from our group and others showed that mutations of $R170^{ECL2}A$ in human CRTH2 (27) and mutations of $H^{3.28}A$, $F^{3.32}A$, $K^{5.42}A$, and $Y^{6.51}A$ in mouse CRTH2 (40) significantly reduced or abolished PGD_2 binding. In addition, the hydroxyl group at C-15 of $15mPGD_2$ forms hydrogen bonds with the side chain of $R170^{ECL2}$ and the main chain carbonyl group of $C182^{ECL2}$; the carbonyl group at C-11 forms a hydrogen bond with the main chain amine group of $C182^{ECL2}$ (Fig. 1*E*). The Δ^{13} carbon–carbon double bond in $15mPGD_2$ is close to the aromatic side chain of $F90^{2.63}$, engaging in potential π–π interactions (Fig. 1*E*).

It has been reported that $15mPGD_2$ is over five times more potent than PGD_2 in inducing cellular signaling events (34), and the inhibitory constant (K_i) value of $15mPGD_2$ in competing antagonist ramatroban is about 20-fold lower than that of PGD_2 (41). CRTH2 also prefers PGD_2 over other endogenous prostaglandins such as PGE_2 (>2,000-fold selectivity) (42). In our structure, the 15-hydroxyl group extends toward $R170^{ECL2}$, because of the *R*-configuration at the C-15 position, to form a hydrogen bond, while in PGD_2 the reversed stereochemical configuration at C-15 position would place the 15-hydroxyl group away from $R170^{ECL2}$, thus breaking the hydrogen-bonding interaction (Fig. 1*E*). Similarly, 15S-methyl-PGD_2 with the *S*-configuration at C-15 also exhibited a much lower affinity for CRTH2 compared to $15mPGD_2$ (34). We further docked PGE_2 into the $15mPGD_2$-binding pocket by superposing a three-dimensional conformer of PGE_2 on top of the $15mPGD_2$ molecule. In the docked structure, both the C-11 and C-15 hydroxyl groups in PGE_2 point toward $F90^{2.63}$ of CRTH2, causing steric hindrance and breaking polar interactions with $R170^{ECL2}$ and $C182^{ECL2}$ of CRTH2 (Fig. 1*F*). This may potentially lead to the lower affinity of PGE_2 for CRTH2 compared to $15mPGD_2$.

Distinctive Lipid Recognition by CRTH2. Recently, structures of several prostaglandin receptors have been reported, including crystal structures of EP3 bound to two prostaglandin agonists, misoprostol and PGE_2, antagonist-bound EP4 and TP, and cryo-EM structures of the EP2–G_s and EP4–G_i complexes with PGE_2 (28–33). The structural comparison of $15mPGD_2$-bound CRTH2 to those structures of other prostanoid receptors reveals significant differences in lipid recognition and receptor activation.

As mentioned in the introductory section, CRTH2 belongs to a different branch of Class A GPCRs compared to other prostanoid receptors. Consequently, the extracellular region of CRTH2 for ligand binding is distinct from that in other prostanoid receptors. In CRTH2, the ECL2 with a β-hairpin structure protrudes from the 7-transmembrane (7-TM) domain and forms a lid domain together with the well-folded N-terminal region to cover the ligand-binding pocket (Fig. 2*A*). In EP2, EP3, EP4, and TP, the ECL2 is buried inside the 7-TM domain, projecting toward TM1 to form the lid domain by itself, which prevents ligand access from the extracellular side (Fig. 2 *B–E*). As a result, PGE_2 binds to its receptors more deeply inside the 7-TM domain compared to $15mPGD_2$ in CRTH2. Interestingly, the orientations of $15mPGD_2$ and PGE_2, relative to their receptors, are also different (Fig. 2). The carboxyl group of $15mPGD_2$ is buried in the distal end of the positively charged ligand-binding pocket of CRTH2, away from TM1 and TM7 (Fig. 2*A*). The positive charge environment is important for PGD_2 binding. Mutations of individual CRTH2 residues $R170^{ECL2}$, $Y184^{ECL2}$, $K210^{5.42}$, and $Y262^{6.51}$ at the distal end of the ligand-binding pocket to the negatively charged glutamic acid led to undetectable PGD_2 binding (*SI Appendix*, Fig. S2). In contrast, in the structures of PGE_2-bound EP2, EP3, and EP4, the carboxyl group of PGE_2 is close to TM1 and TM7, facing the extracellular side of the receptors with the ω-chain extending toward the inside of the 7-TM domain (Fig. 2 *B–D*). Such a binding mode is associated with a predominantly negatively charged environment of the ligand-binding pockets in EP2, EP3, and EP4, which can help to position the carboxyl group of PGE_2 at the top of the ligand-binding pockets through an electrostatic repulsion mechanism (Fig. 2 *B–D*). It is likely that the binding pose of TXA_2 in TP is similar to PGE_2, considering the structural similarity between TP and PGE_2 receptors and the fact that the ligand-binding pocket of TP is also negatively charged (Fig. 2*E*). Supporting distinct lipid recognition mechanisms for CRTH2 and other prostanoid receptors, EP2 residues $R^{7.40}$, $Y^{2.65}$, and T^{ECL2}, that interact with the carboxyl group of PGE_2 are highly conserved in all prostanoid receptors except for CRTH2 (33), while CRTH2 residues, $R170^{ECL2}$, $Y184^{ECL2}$, and $K210^{5.42}$, that form a polar interaction network with the carboxyl group of PGD_2 are not conserved in most of other prostanoid receptors (Fig. 2*F*). Therefore, we propose two lipid recognition modes for the prostanoid receptors, the "polar group in" mode for CRTH2 and the "polar group out" mode for the other prostanoid receptors (Fig. 2*G*). These two lipid-binding modes for the prostanoid receptor family may also apply to other lipid GPCRs as well (see *Discussion*).

The different binding poses of lipid agonists in CRTH2 and other prostanoid receptors also suggest nonconserved mechanisms of receptor activation. The structure of EP3 bound to PGE_2 represents an active-like conformational state, characterized by an outward displacement of the cytoplasmic end of TM6

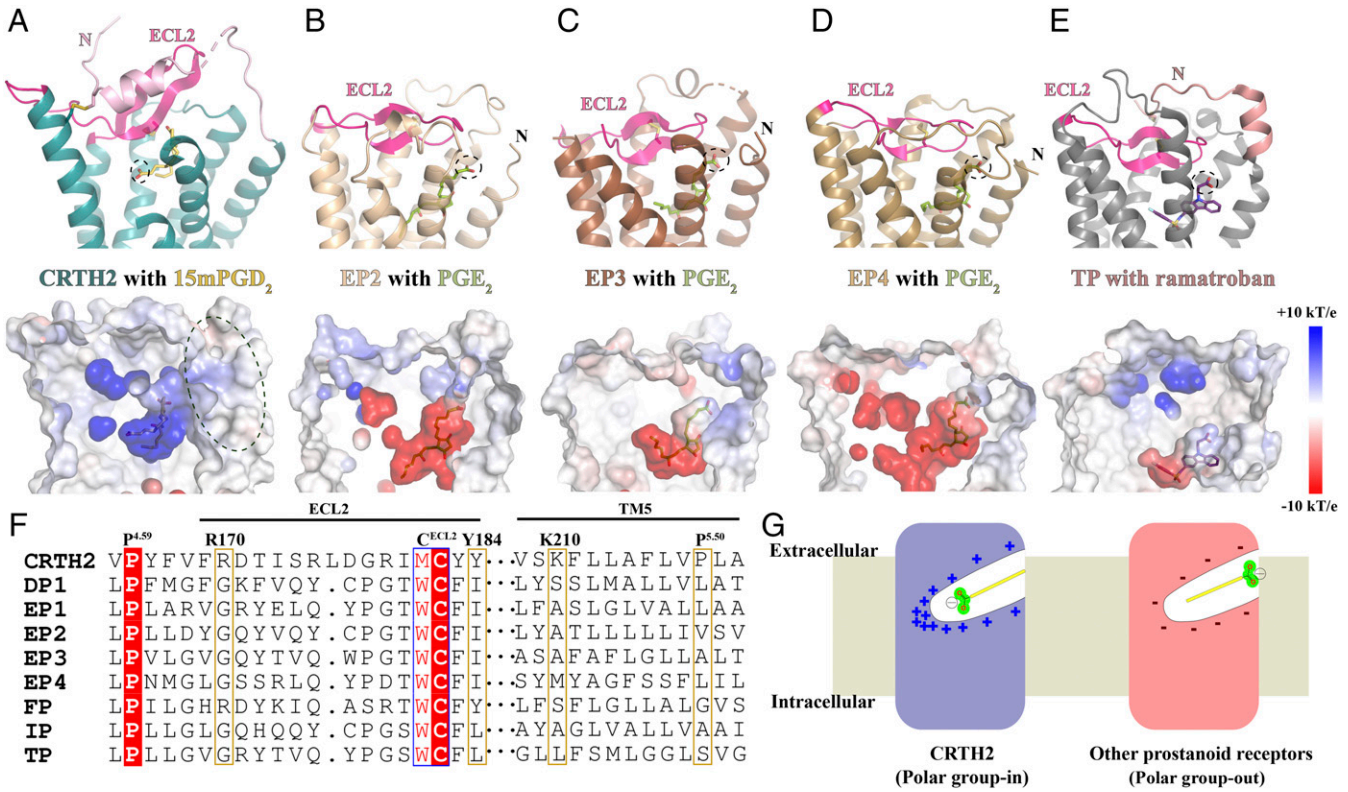

Fig. 2. Structural comparison analysis. (*A*) CRTH2 with 15mPGD$_2$. The N-terminal region preceding TM1 is colored in light pink. (*B–D*) EP2, EP3, and EP4 with PGE$_2$ (Protein Data Bank [PDB] IDs: 7CX2, 6AK3, and 7D7M, respectively). (*E*) TP with ramatroban (PDB ID: 6IIU). The N-terminal region preceding TM1 is colored in salmon. ECL2 in each receptor is colored in magenta. 15mPGD$_2$, PGE$_2$, and ramatroban are colored in yellow, green, and purple, respectively. The carboxyl group in each ligand is circled. The charge distributions of ligand-binding pockets of these prostanoid receptors are shown in the lower panels. (*F*) Sequence alignment of all prostanoid receptors. The alignment of ECL2 sequences was based on the alignments of two highly conserved residues, P$^{4.50}$ and the cysteine residue, in ECL2, forming the conserved extracellular disulfide bond. The alignment of TM5 sequences was based on the alignment of 5.50 residues in the receptors. (*G*) Two lipid-binding modes.

starting at W$^{6.48}$ in comparison to antagonist-bound EP4 (30). In the EP3–PGE$_2$ structure, the end of the ω-chain of PGE$_2$ extends toward TM6, forming hydrophobic interactions with residues L298$^{6.51}$ and W295$^{6.48}$ (Fig. 3*A*). It has been proposed that the direct contact of the ω-chain of PGE$_2$ with W$^{6.48}$ and surrounding residues is important for the activation of the receptor (30). Indeed, previous studies on other GPCRs suggested that W$^{6.48}$ functions as a "toggle switch" or a part of a "transmission switch" with F$^{6.44}$ that links the ligand binding at the extracellular region to the activation of the receptor at the cytoplasmic region (43, 44). For EP2 and EP4, the conserved W$^{6.48}$ is replaced by S$^{6.48}$ (31–33). Structural studies on the EP2 signaling complex with PGE$_2$ suggested that a direct interaction between the ω-chain of PGE$_2$ and M124$^{3.40}$ instead of W$^{6.48}$, which packs against F273$^{6.44}$, may stabilize the active conformation of EP2 (33) (Fig. 3*B*). In CRTH2, the lipid agonist 15mPGD$_2$ binds to a much more superficial binding pocket compared to PGE$_2$, and it does not directly interact with the F$^{6.44}$xxCW$^{6.48}$ motif (Fig. 3*C*).

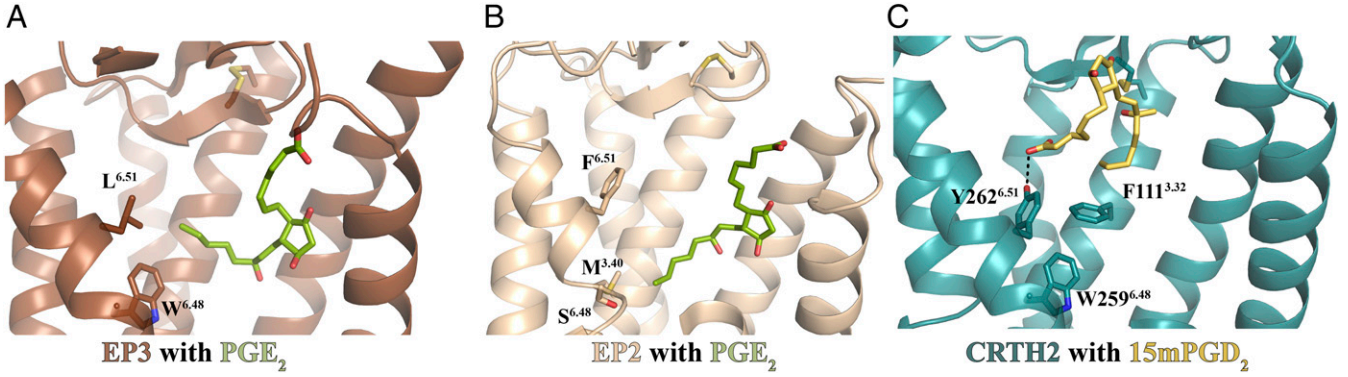

Fig. 3. PGE$_2$ and PGD$_2$ interact with different sets of residues to activate their receptors. (*A*) EP3 (brown) with PGE$_2$ (green) (PDB ID: 6AK3). (*B*) EP2 (light brown) with PGE$_2$ (green) (PDB ID: 7CX2). The ω-chain of PGE$_2$ extends below the 6.51 residue to interact with W295$^{6.48}$ in EP3 or M124$^{3.40}$ in EP2. (*C*) CRTH2 (cyan) with 15mPGD$_2$ (yellow). PGD$_2$ binds to a superficial binding pocket in CRTH2 so that the ω-chain of PGD$_2$ is above the residue Y$^{6.51}$. The hydrogen bond is shown as a black dashed line.

In the U shape–binding pose of 15mPGD$_2$, the carboxyl group forms a hydrogen bond with Y262$^{6.51}$, and the ω-chain points toward TM3, forming a hydrophobic interaction with F111$^{3.32}$. Both Y262$^{6.51}$ and F111$^{3.32}$, in turn, pack against W259$^{6.48}$ (Fig. 3*C*). This implies a distinct activation mechanism of CRTH2 compared to the PGE$_2$ receptors, which may involve residues Y262$^{6.51}$, F111$^{3.32}$, and W259$^{6.48}$.

Potential Lipid-Binding Process Revealed by MD Simulations. To explore the conformational dynamics associated with the lipid-bound CRTH2, we carried out equilibrium molecular dynamics (MD) simulations of CRTH2 in its ligand-free (apo) and 15mPGD$_2$-bound (holo) states. We generated four independent 1-μs trajectories of CRTH2 embedded in TIP3P-solvated 1-palmitoyl-2-oleoyl-*sn*-glycero-3-phosphocholine (POPC) bilayers, two in apo (apo-1 and apo-2) and two in holo states (holo-1 and holo-2). The system preparation and MD simulation protocol are described in the *Materials and Methods* section. All four trajectories remained stable over the 1-μs simulation, with the receptor in the holo-1 system exhibiting relatively larger conformational deviations, as compared to the other three systems (*SI Appendix*, Fig. S3). In all four simulation systems, the receptor mainly stayed in the inactive conformation, as in the crystal structure. We analyzed the tilt of the seven transmembrane helices TM1 to TM7 and helix 8 with respect to the normal to the plane of the membrane (*z*-axis) and observed no major conformational changes of the transmembrane helices. The average tilt angles remained close to those observed in the crystal structure in all four systems during the course of the simulation (*SI Appendix*, Fig. S4). The SD values for the tilt angles of all seven transmembrane helices were in the range of 0.8 to 2.3° only, suggesting that there were no significant shifts in their relative orientations. In contrast, H8 in all four trajectories showed significant shifts in the tilt angle (*SI Appendix*, Fig. S4).

In contrast to the subtle conformational changes of the transmembrane helices, the 15mPGD$_2$ molecule in both holo simulations showed significant rearrangements during the simulation compared to its initial conformation (Fig. 4 *A* and *B*). In holo-1, the conformational changes associated with the bound 15mPGD$_2$ molecule were relatively subtle compared to those observed in holo-2, with its anionic headgroup rearranged but still interacting directly with R170^{ECL2} and its aliphatic ω-chain wedged between TM2 and TM3 (Fig. 4 *A* and *C*). In contrast to the subtle changes of 15mPGD$_2$ in holo-1, in holo-2, 15mPGD$_2$ exhibited dramatic changes with respect to its initial conformation. The molecule adopted a more linear conformation, in contrast to the U-shaped conformation in the crystal structure. The anionic headgroup of 15mPGD$_2$ moved away from both R170^{ECL2} and K210$^{5.42}$ toward the extracellular side to form new interactions with R175^{ECL2}, which was accompanied by a displacement of the N-helix toward the extracellular milieu (Fig. 4 *B* and *D*). This partial dissociation of 15mPGD$_2$ may represent an intermediate state in the ligand-binding/unbinding processes.

The subtle movement of 15mPGD$_2$ in holo-1 was associated with binding of a POPC molecule from the lipid bilayer to CRTH2, which potentially hindered the partial dissociation of 15mPGD$_2$, as that observed in holo-2. In holo-1, the POPC molecule, POPC330, moved toward ECL2 through the putative entry port between TM1 and TM7. At t = 0 ns, POPC330 was positioned near the entry port with one of its acyl chains wedged between TM1 and TM7 (*SI Appendix*, Fig. S5*A*). In this position, the phosphate group of POPC330 was in close proximity of charged/polar residues lining the entry port, including D32$^{1.32}$, R284$^{7.32}$, and H95^{ECL1} at the water–bilayer interface, while the acyl chains were flanked by hydrophobic residues from TM1 and TM7. The cleft formed by TM1 and TM7 has been shown to be a high-occupancy site for phospholipids in atomistic and coarse-grained simulations of β$_2$-adrenergic (45) and serotonin$_{1A}$ receptors (46), along with the role of membrane cholesterol in regulating the occupancy of the TM1 to TM7 cleft (47). Over the course of the simulation in holo-1, the phosphate group of POPC330 formed salt bridges and hydrogen bonds with H95^{ECL1}, R284$^{7.32}$, and R179^{ECL2}, causing the POPC headgroup to be laterally pulled toward ECL2 from the bilayer by ∼7 Å along the membrane plane (Fig. 5 *A* and *B* and *SI Appendix*, Fig. S5*B*). The phosphate group initially formed transient salt–bridge interactions with R179^{ECL2} and/or R284$^{7.32}$. Subsequently, the interaction with R179^{ECL2} was stabilized, allowing the POPC headgroup to move further inward and, in turn, establish an interaction with R175^{ECL2} (Fig. 5*C*). No such inward movement of a bilayer POPC molecule was observed in the other three trajectories, despite the presence of a POPC molecule near the entry port at t = 0 ns in those systems (*SI Appendix*, Fig. S5). In order to accommodate the inward movement of the headgroup and acyl chains of the captured POPC, TM1 moved away from TM7, increasing the space within the entry port.

The binding of 15mPGD$_2$ and POPC330 near the bilayer–water interface observed in the two holo simulations may be suggestive of how CRTH2 captures anionic lipid ligands. We propose that the "cationic tetrad" of R284$^{7.32}$, H95^{ECL1}, R179^{ECL2}, and R175^{ECL2}, which line at the ligand entry port and do not directly interact with CRTH2 antagonists (27) or 15mPGD$_2$ in the crystal structures, constitute a lipid trap to enable the initial capture of anionic eicosanoid lipids from the cell membrane. Previous studies showed that mutation of R178^{ECL2} to Ala in mouse CRTH2, which corresponds to R179^{ECL2} in human CRTH2, significantly decreased the affinity of PGD$_2$ for CRTH2 (40). We also performed ^{3}H-PGD$_2$ saturation–binding assays on CRTH2 mutants R175^{ECL2}A, H95^{ECL1}A, and R284$^{7.32}$A (Fig. 5*D*). All mutants showed comparable expression levels as the wtCRTH2 (*SI Appendix*, Fig. S6), with compromised PGD$_2$ binding. The results suggested the important roles of these residues in PGD$_2$ binding, supporting our proposed, lipid-capturing mechanism. Interestingly, the side chains of R175^{ECL2} and R179^{ECL2}, despite being cationic, maintained their proximity and almost parallel orientation to each other in all four trajectories without any electrostatic repulsion. This was due to the presence of an anionic residue, D177^{ECL2}, between R175^{ECL2} and R179^{ECL2} (Fig. 5*B* and *SI Appendix*, Fig. S7), potentially circumventing any repulsion between the two residues. Therefore, we further propose that D177^{ECL2} functions as the foil to help maintain the proper orientation of the two cationic residues, which in turn allows the effective capturing of anionic eicosanoid lipids. The vital role of D177^{ECL2} in PGD$_2$ binding was confirmed by mutagenesis study (Fig. 5*D* and *SI Appendix*, Fig. S6).

Conformational Dynamics of CRTH2 in MD Simulations. The tetrad of R284$^{7.32}$, H95^{ECL1}, R179^{ECL2}, and R175^{ECL2} is centered around the entry port at the water–bilayer interface, ∼19 Å away from R170^{ECL2} and K210$^{5.42}$ in the binding pocket. Once captured, how the anionic group of the ligand is translocated across such a distance toward R170^{ECL2} and K210$^{5.42}$ is unclear. Our simulation studies show that the binding pocket of CRTH2 undergoes structural rearrangements, leading to significant changes in residue packing. We characterized the residue packing changes within the binding site in the simulations by calculating the radius of gyration of the binding pocket (Fig. 6*A*). We defined the binding pocket by considering those residues that are within 5.0 Å of the 15mPGD$_2$ molecule in the crystal structure. The analysis shows that the removal of the bound 15mPGD$_2$ in apo simulations causes the packing within the pocket to relax, causing it to open up (Fig. 6*A*). Similar relaxation of the binding site residue packing is also observed in holo simulations but to a lesser magnitude, relative to the apo simulations. In holo-2, the brief spike in the radius of gyration at t ∼150 ns corresponds to the 15mPGD$_2$-unbinding event. The changes in residue packing can be attributed to conformational changes associated with M17$^{N\text{-helix}}$, W283$^{7.31}$, and Y183^{ECL2} and the interactions between

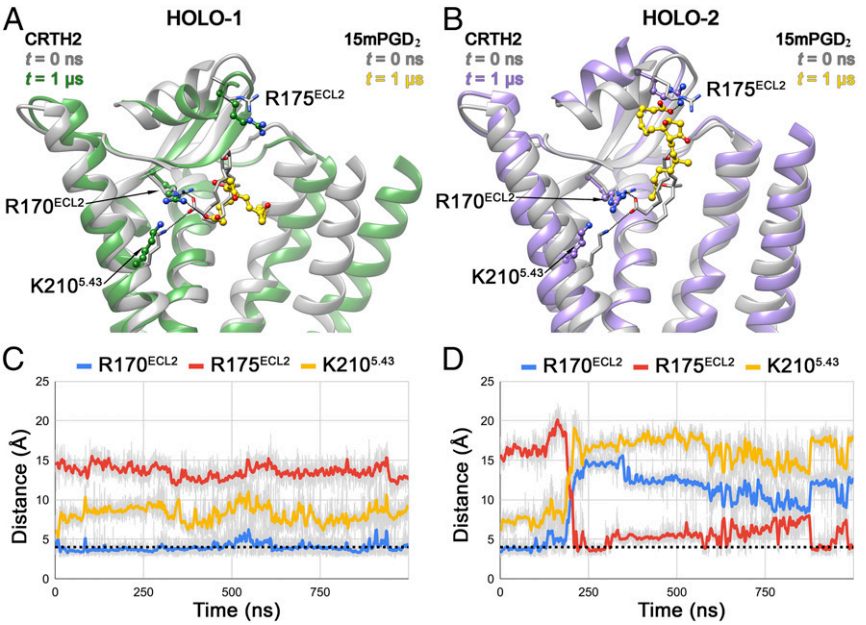

Fig. 4. Conformational dynamics of 15mPGD$_2$ in CRTH2 holo-1 and holo-2 systems. The CRTH2 structures at $t = 0$ ns (translucent gray ribbon) are superposed with structures at $t = 1$ μs in holo-1 (*A*) (translucent green ribbon) and $t = 1$ μs in holo-2 (*B*) (translucent purple ribbon). In both panels, conformations of bound 15mPGD$_2$ at $t = 0$ ns (translucent gray) and $t = 1$ μs (gold) are shown in stick and ball-and-stick representation, respectively. Salt–bridge interactions formed by the carboxyl group of 15mPGD$_2$ with R170^{ECL2}, R175^{ECL2}, and K210$^{5.42}$ are shown as black dotted lines in *A* and *B*. Evolution of the salt bridges during the 1-μs simulation in holo-1 (*C*) and holo-2 (*D*) systems are presented as blue, red, and yellow lines (50-point moving average) corresponding to 15mPGD$_2$-R170^{ECL2}, 15mPGD$_2$-R175^{ECL2}, and 15mPGD$_2$-K210$^{5.42}$ interactions, respectively, with the dotted black line indicating the cutoff distance of 4.0 Å.

these residues (Fig. 6*A*). In the crystal structure, the N-helix is nestled between the extracellular end of TM7 and ECL2, with M17$^{N\text{-helix}}$ forming numerous contacts with the surrounding residues. In particular, the side chain of M17$^{N\text{-helix}}$ is flanked by W283$^{7.31}$ and Y183^{ECL2} and is buried within the upper half of the binding pocket (*SI Appendix*, Fig. S8). Such an arrangement of these three residues is reminiscent of an Aro-Met-Aro "bridging" motif and is likely mediated by S-π/CH-π–type interactions (48). Such Met-aromatic interactions are abundant in protein structures (48–51).

We observed the disruption of the bridging motif characterized by the breakage of W283$^{7.31}$–M17$^{N\text{-helix}}$ and/or Y183^{ECL2}–M17$^{N\text{-helix}}$ interactions (Fig. 6 *B* and *C*) in all four simulations, resulting in the disorganization of the tightly packed hydrophobic interaction network involving the extracellular end of TM7, N-helix, and ECL2. We characterized the bridge disruption by scrutinizing the distribution of W283$^{7.31}$–M17$^{N\text{-helix}}$ distances and W283$^{7.31}$ χ1 rotamer angles. In the crystal structure, the W283$^{7.31}$ side chain is pointed inwards (χ1 = –57.6°), favoring the formation of the W283$^{7.31}$–M17$^{N\text{-helix}}$–Y183^{ECL2} bridge motif. However, in all simulations except holo-2, W283$^{7.31}$ side chain flips outwards (χ1 ~180°), breaking the W283$^{7.31}$–M17$^{N\text{-helix}}$ interaction and leading to the bridge disruption (Fig. 6 *D*–*G*). As a consequence, the N-helix moves away from the TM core (Fig. 6 *H*–*K*), associated with an increase in the volume of the translocation channel. In selected representative conformations of CRTH2, the disruption of the bridge motif culminates in the increase of volume of the translocation pathway from 1,435 Å^3 (apo-1 at $t = 0$ ns) to 2,626 Å^3, 2,345 Å^3, 1,773 Å^3, and 1,786 Å^3 in apo-1, apo-2, holo-1, and holo-2 simulations, respectively (*SI Appendix*, Fig. S9).

Based on this observation, we hypothesized that the bridging motif mediated by M17$^{N\text{-helix}}$ might be of critical importance for ligand binding. Abrogation of the W283$^{7.31}$–M17$^{N\text{-helix}}$–Y183^{ECL2} bridging motif by mutation M17$^{N\text{-helix}}$A disrupts PGD$_2$ binding (Fig. 5*D*), confirming the important role of M17$^{N\text{-helix}}$ in PGD$_2$ binding. Considering the CRTH2–POPC interactions in holo-1, the sequence of events leading to the ligand unbinding in holo-2, and the associated changes in the bridging motif anchored by M17$^{N\text{-helix}}$, we speculate that the holo simulations represent potential transitional states in the ligand-binding process: holo-1 gives glimpses into the initial ligand-binding events, while holo-2 shows stages of ligand unbinding. Collectively, our observations suggest that the translocation of the anionic lipid ligand toward the binding pocket is modulated by the dynamics of the N-helix mediated by M17$^{N\text{-helix}}$.

Discussion

Previously reported structures of CRTH2 bound to antagonists revealed a nonuniform positive charge distribution in the ligand-binding pocket, which has been suggested to guide the carboxylate group of CRTH2 lipid ligands to reach the distal end by opposite charge attraction (27). Indeed, the structure of CRTH2 bound to 15mPGD$_2$ confirms that the carboxylate group of 15mPGD$_2$ resides at the distal end of the ligand-binding pocket, with the highest positive charge distribution, forming polar interactions with R170^{ECL2} and K210$^{5.42}$, both of which have been shown to be critical for PGD$_2$ binding (27, 40). The U shape lipid–binding mode explains well the selectivity of CRTH2 for different lipid ligands.

The polar group in–binding mode of PGD$_2$ on CRTH2 contrasts the polar group out–binding modes of lipid ligands on other prostanoid receptors. These two distinct lipid-binding modes may also apply to other lipid GPCRs. For example, structures of sphingosine-1–phosphate receptor 1, lysophosphatidic acid receptor 1, and cannabinoid receptors revealed negatively charged, ligand-binding pockets associated with polar group out–binding modes of their lipid ligands (27). Interestingly, these GPCRs and all prostanoid receptors except CRTH2 belong to the α-branch of Class A GPCRs (6). On the other hands, crystal structures of cysteinyl leukotriene receptors (CLTRs) (52, 53) revealed positively charged, ligand-binding pockets with uneven charge distribution, similar to that of CRTH2 (*SI Appendix*, Fig. S10). In addition, the carboxylate group

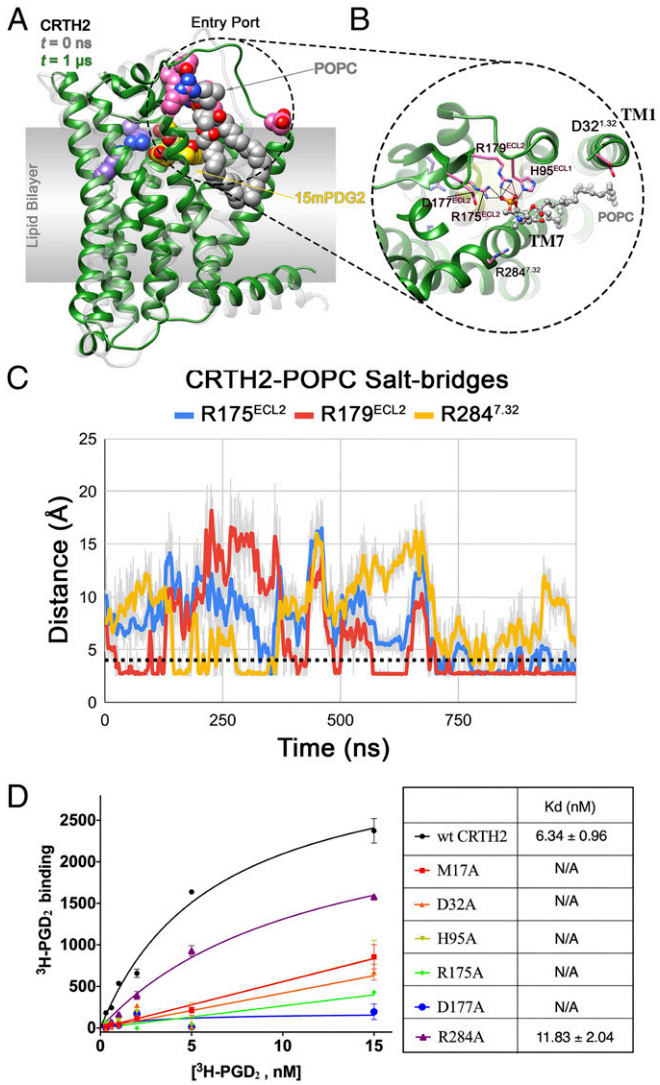

Fig. 5. CRTH2–POPC interaction in holo-1 simulation and mutagenesis data. (*A*) Interaction of a bilayer POPC molecule, with the residues lining the entry port in holo-1 simulation. The structures of the receptor at $t = 0$ ns (translucent gray) and $t = 1$ μs (green) are shown in ribbon representation. The entry port residues (pink), bound 15mPGD$_2$ (yellow), POPC (gray), and binding site residues R170^{ECL2} and K210$^{5.42}$ (purple) are shown in sphere representation. (*B*) Close up of the CRTH2 entry port–POPC interaction, with the bound POPC (gray) and entry port residues (pink) shown in ball-and-stick and stick representation, respectively. The interactions between the POPC and the protein residues are shown as black dotted lines. (*C*) Evolution of CRTH2–POPC intermolecular salt bridges during the 1-μs holo-1 simulation, with the dotted black line indicating the cutoff distance of 4.0 Å. (*D*) Saturation-binding assays on different CRTH2 constructs using ^{3}H-PGD$_2$. All CRTH2 constructs were transiently expressed in human embryonic kidney 293 cells, and cell membranes were prepared and used in the ligand-binding assays. Expression of each construct was confirmed by cell surface staining. Nonspecific binding measured in the presence of access amount of PGD$_2$ was subtracted. The dissociation equilibrium constants (K_ds) of PGD$_2$ for the wtCRTH2 and the R284A mutant are listed in the table shown on the right of panel *D*. For other CRTH2 mutants, no saturable ^{3}H-PGD$_2$ binding was observed, indicating mostly nonspecific binding. Each data point in the left panel is shown as mean ± SEM and $n = 3$.

of cysteinyl LTD$_4$ has been proposed to be buried inside the binding pocket of CLTR1 (53), adopting a polar group in–binding mode. Therefore, it is likely that cysteinyl leukotrienes enter the lipid-binding pockets of CLTRs through a similar opposite charge attraction-facilitated mechanism, although the potential ligand entrance in CLTRs is different from that in CRTH2 (53).

To study the conformational dynamics of the human CRTH2, we carried out equilibrium MD simulations of the receptor in its apo and holo states. In our simulations, the receptor structure in holo systems in the presence of the agonist 15mPGD$_2$ did not exhibit or assume any active-like conformations with respect to the intracellular end of TM6 or other conserved GPCR structural motifs. However, conformations sampled by CRTH2 in our MD simulation studies, coupled with functional assays of receptor mutants, helped us identify the roles of critical residues that were hitherto unrecognized or merely speculated upon. Holo simulations provided glimpses into the nature of the ligand-binding/unbinding process and the associated, conformational changes there within. The observed interaction of a bilayer POPC molecule with CRTH2 led to the identification of the mechanistic role of the cationic tetrad in the initial ligand capture process. Our study highlights the cooperative effects of the cationic tetrad R284$^{7.32}$, R175^{ECL2}, R179^{ECL2}, and H95^{ECL1}, which act like fishhooks that aid in picking out anionic group-containing lipids from the membrane, with D32$^{1.32}$ potentially funneling the ligands toward the entry port. All of these residues at the ligand entry port do not directly interact with 15mPGD$_2$ in the crystal structure; however, our mutagenesis studies confirmed their important roles in lipid recognition (Fig. 5*D*). In FPR2, the residue at position 7.32 (D282$^{7.32}$) has been suggested to be important for interaction with short formylpeptides with cationic, terminal moieties (54, 55). Also, a similar fishhook-like role for a cationic residue in the capture of a lipid-like substrate has been suggested for the bacterial lysophospholipid transporter (56). Therefore, the role of the cationic tetrad and its interactions with anionic lipids in CRTH2 could potentially represent a common mechanism employed by certain GPCRs and other membrane proteins. Our studies also shed light on the mechanisms involved in the stabilization and orientation of the cationic tetrad, especially R175^{ECL2} and R179^{ECL2}. One of the distinct features present in CRTH2 is the ordered N-terminal region, and our study addresses one of the potential roles of the N-helix in modulating the access to the binding pocket and its packing via the W283$^{7.31}$–M17$^{N\text{-helix}}$–Y183^{ECL2} bridge motif. Breaking of either or both W283$^{7.31}$–M17$^{N\text{-helix}}$ and M17$^{N\text{-helix}}$–Y183^{ECL2} S-π–type interactions displaces the W283$^{7.31}$ and M17$^{N\text{-helix}}$ side chains from the binding pocket. Such a disruption increases the volume of the binding pocket in the simulations and could facilitate ligand binding/unbinding.

Based on our computational and experimental findings, we propose the following mechanistic model for the anionic, lipid-binding process in CRTH2. We postulate that electrostatically driven interactions with residues of the cationic tetrad R284$^{7.32}$, R175^{ECL2}, R179^{ECL2}, and H95^{ECL1}, potentially assisted by D32$^{1.32}$, favor the initial capture of anionic, lipid-like ligands and their subsequent inward transition from the bilayer. Following the initial binding and lateral inward movement of the anionic group, the receptor could shift through transitional conformations, as observed in the holo simulations. Once the ligand anionic group is optimally positioned, the complete/partial reestablishment of the bridging motif W283$^{7.31}$–M17$^{N\text{-helix}}$–Y183^{ECL2} could facilitate the movement of the anionic group into the binding pocket of the receptor toward R170 and K210, establishing the ligand-bound conformation, as observed in the crystal structure.

Materials and Methods

Protein Expression, Purification, and Crystallization. CRTH2 was engineered, expressed in insect Sf9 cells, and purified in complex with 15mPGD$_2$, as previously described (27). Microcrystals (5 to 10 μm) for SFX were grown in LCP inside 100-μL gas-tight syringes, as previously described (57), and then transported to XFEL for data collection. During sample transportation to XFEL, the LCP in all syringes converted into a sponge phase. The sponge

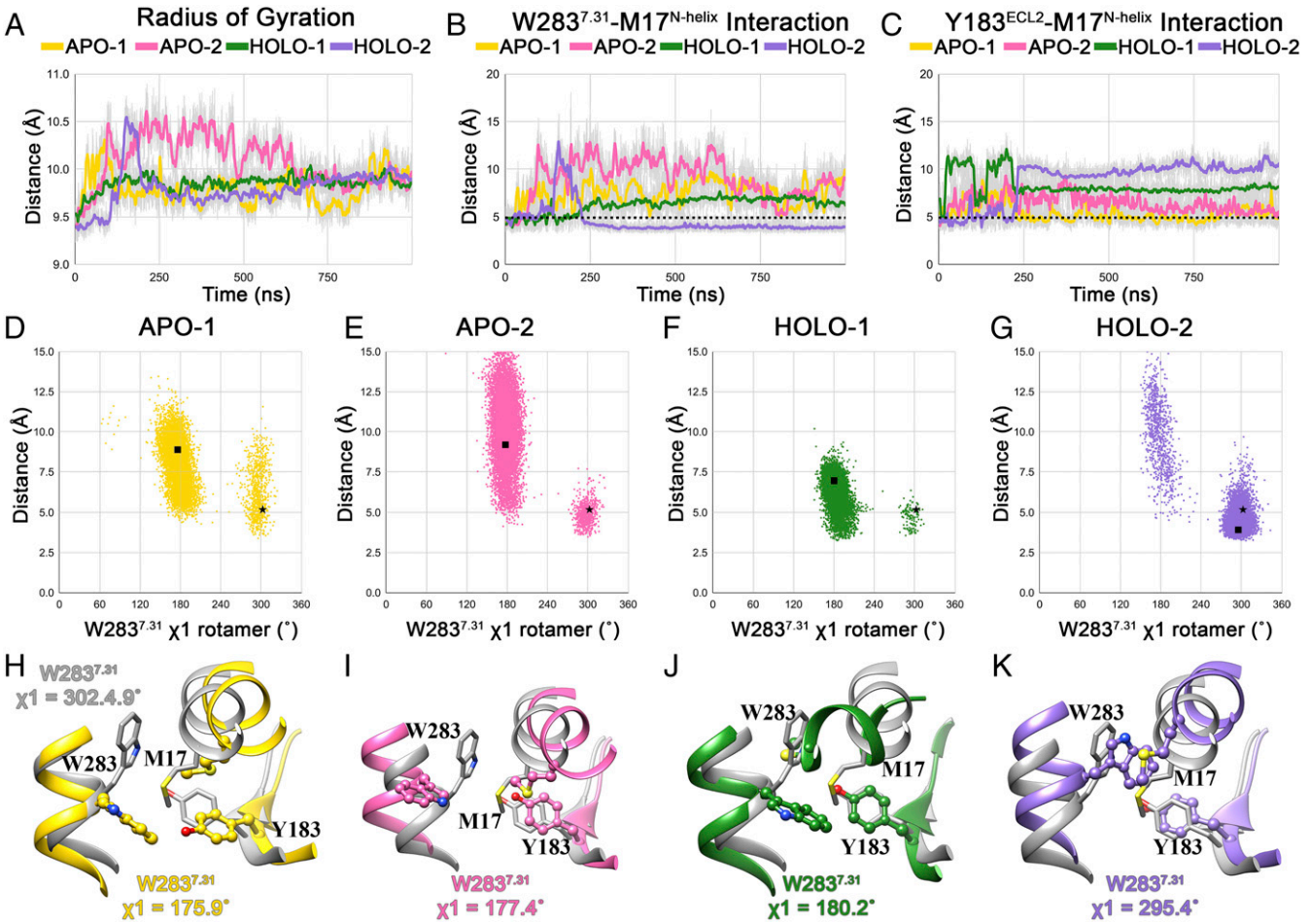

Fig. 6. Conformational dynamics of the ligand-binding pocket in MD simulations. (*A*) Evolution of radius of gyration (50-point moving average) of the binding site residues in 1-μs trajectories. Evolution of S-π–type $W283^{7.31}$–$M17^{N\text{-helix}}$ (*B*) and $Y183^{ECL2}$–$M17^{N\text{-helix}}$ (*C*) interactions in 1-μs trajectories. Scatter plot showing distribution of $W283^{7.31}$ (ring centroid)–$M17^{N\text{-helix}}$ (S-atom) distances and $W283^{7.31}$ $\chi1$ rotamer angles in $W283^{7.31}$ apo-1 (*D*), apo-2 (*E*), holo-1 (*F*), and holo-2 (*G*) trajectories. Structures with $W283^{7.31}$ $\chi1$ rotamer angle equal to the average $W283^{7.31}$ $\chi1$ rotamer angle in the last 500 ns of the simulation are selected as representatives from each trajectory. The distance and $\chi1$ rotamer angle corresponding to the crystal structure and representative structure from each simulation are shown using a black star and square in the scatter plots. Organization of the $W283^{7.31}$–$M17^{N\text{-helix}}$–$Y183^{ECL2}$ bridge motif in representative structures, along with their $W283^{7.31}$ $\chi1$ rotamer angle, from apo-1 (*H*) (yellow), apo-2 (*I*) (pink), holo-1 (*J*) (green), and holo-2 (*K*) (purple) trajectories. The bridge motif from the crystal structure (gray) is also shown superposed to the representative structure.

phase with crystals was carefully separated from the precipitant and converted back into LCP for injection in the XFEL beam. Details of protein production and sample preparation for the SFX are described in *SI Appendix*.

Diffraction Data Collection and Structure Determination. SFX data were collected at the coherent X-ray imaging instrument (58) of the Linac Coherent Light Source (LCLS). A total of 850,000 images were recorded within ∼2 h using ∼50 μL sample. A total of 20,358 potential, single-crystal diffraction patterns (crystal hits) were identified using Cheetah (59). Indexing, integration, and merging of the crystal diffraction data were performed using CrystFEL (60). The final dataset was analyzed by the STARANISO webserver (61) and truncated to 3.2, 3.2, and 2.6 Å resolution along the reciprocal unit cell vectors a*, b*, and c*, respectively. The structure was solved by the molecular replacement method. Final data collection and refinement statistics are shown in Table 1. Details of data collection and structure determination are described in *SI Appendix*.

Radioligand-Binding Assay and Protein Surface Expression. The expression levels of wtCRTH2 and mutants in human embryonic kidney 293 (HEK293) cells were determined by flow cytometry experiments (*SI Appendix*). Binding assays were performed using cell membranes expressing CRTH2 and mutants in the presence of the radioactive ^{3}H-PGD_2 and nonradioactive PGD_2 or 15mPGD_2 (*SI Appendix*).

MD Simulations. Apo or holo configurations of CRTH2 were embedded into a TIP3P-solvated bilayer comprising 300 POPC molecules. The systems were neutralized by adding Na^+ and Cl^- ions. The protein, solvent, lipids, and ions were modeled using CHARMM36 force-field parameters (62). Initial parameters for the 15mPGD_2 molecule were generated using CHARMM general force field [CGenFF (63)] implemented through the ParamChem (64, 65) web server and were further refined using the GAAMP (63) web server. Details are described in *SI Appendix*.

All simulations were performed using GROMACS version 5.1.2 (66). Long-range electrostatics were calculated with the particle mesh Ewald scheme, while a 12-Å cutoff was employed for estimating short-range, nonbonded interactions. After energy minimization, the systems were equilibrated by applying harmonic position restraints on nonsolvent heavy atoms, which were gradually reduced over six equilibration steps (details in *SI Appendix*). All restraints were removed postequilibration and 1 μs production runs were carried out at 303.15 K (Nośe–Hoover thermostat) and 1.0 bar pressure (Parrinello–Rahman barostat). Covalent bonds were constrained with linear constraint solver algorithm (67). Pressure coupling was applied semiisotropically during NPT equilibration steps and unrestrained production runs.

Analysis of MD Simulation Trajectories. The analysis is described in *SI Appendix*.

Data Availability. Atomic coordinates and structure factors for the structure of 15mPGD_2–CRTH2 have been deposited in the Protein Data Bank with the

accession code 7M8W. All other study data are included in the article and/or supporting information.

ACKNOWLEDGMENTS. R.N.V.K.D. and H.F. gratefully acknowledge the Biomedical Research Council, A*STAR for financial support. The computational work for this article was partially performed on resources of the National Supercomputing Centre, Singapore (https://www.nscc.sg). U.W., H.H., and V.C. acknowledge financial support from the Science and Technology Center Program of the NSF through BioXFEL under Agreement No. 1231306. Use of the LCLS, Stanford Linear Accelerator Center National Accelerator Laboratory, is supported by the US Department of Energy, Office of Science, Office of Basic Energy Sciences under Contract No. DE-AC02-76SF00515. C.Z. is supported by Grant No. R35GM128641 from the National Institute of General Medical Sciences, NIH of the United States.

1. J. A. Boyce, Eicosanoids in asthma, allergic inflammation, and host defense. *Curr. Mol. Med.* **8**, 335–349 (2008).
2. H. Harizi, J.-B. Corcuff, N. Gualde, Arachidonic-acid-derived eicosanoids: Roles in biology and immunopathology. *Trends Mol. Med.* **14**, 461–469 (2008).
3. C. D. Funk, Prostaglandins and leukotrienes: Advances in eicosanoid biology. *Science* **294**, 1871–1875 (2001).
4. M. Bäck *et al.*, International Union of Basic and Clinical Pharmacology. LXXXIV: Leukotriene receptor nomenclature, distribution, and pathophysiological functions. *Pharmacol. Rev.* **63**, 539–584 (2011).
5. D. F. Woodward, R. L. Jones, S. Narumiya, International Union of Basic and Clinical Pharmacology. LXXXIII: Classification of prostanoid receptors, updating 15 years of progress. *Pharmacol. Rev.* **63**, 471–538 (2011).
6. R. Fredriksson, M. C. Lagerström, L.-G. Lundin, H. B. Schiöth, The G-protein-coupled receptors in the human genome form five main families. Phylogenetic analysis, paralogon groups, and fingerprints. *Mol. Pharmacol.* **63**, 1256–1272 (2003).
7. K. Nagata, H. Hirai, The second PGD(2) receptor CRTH2: Structure, properties, and functions in leukocytes. *Prostaglandins Leukot. Essent. Fatty Acids* **69**, 169–177 (2003).
8. K. Nagata *et al.*, Selective expression of a novel surface molecule by human Th2 cells in vivo. *J. Immunol.* **162**, 1278–1286 (1999).
9. L. Cosmi *et al.*, CRTH2 is the most reliable marker for the detection of circulating human type 2 Th and type 2 T cytotoxic cells in health and disease. *Eur. J. Immunol.* **30**, 2972–2979 (2000).
10. J. M. Mjösberg *et al.*, Human IL-25- and IL-33-responsive type 2 innate lymphoid cells are defined by expression of CRTH2 and CD161. *Nat. Immunol.* **12**, 1055–1062 (2011).
11. H. Hirai *et al.*, Prostaglandin D2 selectively induces chemotaxis in T helper type 2 cells, eosinophils, and basophils via seven-transmembrane receptor CRTH2. *J. Exp. Med.* **193**, 255–261 (2001).
12. G. Monneret, S. Gravel, M. Diamond, J. Rokach, W. S. Powell, Prostaglandin D2 is a potent chemoattractant for human eosinophils that acts via a novel DP receptor. *Blood* **98**, 1942–1948 (2001).
13. L. Xue *et al.*, Prostaglandin D2 causes preferential induction of proinflammatory Th2 cytokine production through an action on chemoattractant receptor-like molecule expressed on Th2 cells. *J. Immunol.* **175**, 6531–6536 (2005).
14. E. Kostenis, T. Ulven, Emerging roles of DP and CRTH2 in allergic inflammation. *Trends Mol. Med.* **12**, 148–158 (2006).
15. E. D. Tait Wojno *et al.*, The prostaglandin D_2 receptor CRTH2 regulates accumulation of group 2 innate lymphoid cells in the inflamed lung. *Mucosal Immunol.* **8**, 1313–1323 (2015).
16. C. Pelaia *et al.*, New treatments for asthma: From the pathogenic role of prostaglandin D_2 to the therapeutic effects of fevipiprant. *Pharmacol. Res.* **155**, 104490 (2020).
17. M. Kupczyk, P. Kuna, Targeting the PGD_2/CRTH2/DP1 signaling pathway in asthma and allergic disease: Current status and future perspectives. *Drugs* **77**, 1281–1294 (2017).
18. N. Barnes *et al.*, A randomized, double-blind, placebo-controlled study of the CRTH2 antagonist OC000459 in moderate persistent asthma. *Clin. Exp. Allergy* **42**, 38–48 (2012).
19. V. J. Erpenbeck *et al.*, The oral CRTh2 antagonist QAW039 (fevipiprant): A phase II study in uncontrolled allergic asthma. *Pulm. Pharmacol. Ther.* **39**, 54–63 (2016).
20. P. Kuna, L. Bjermer, G. Tornling, Two phase II randomized trials on the CRTh2 antagonist AZD1981 in adults with asthma. *Drug Des. Devel. Ther.* **10**, 2759–2770 (2016).
21. E. D. Bateman *et al.*, Fevipiprant, an oral prostaglandin DP_2 receptor (CRTh2) antagonist, in allergic asthma uncontrolled on low-dose inhaled corticosteroids. *Eur. Respir. J.* **50**, 1700670 (2017).
22. D. Miller *et al.*, A randomized study of BI 671800, a CRTH2 antagonist, as add-on therapy in poorly controlled asthma. *Allergy Asthma Proc.* **38**, 157–164 (2017).
23. H. Ortega *et al.*, A phase 2 study to evaluate the safety, efficacy and pharmacokinetics of DP2 antagonist GB001 and to explore biomarkers of airway inflammation in mild-to-moderate asthma. *Clin. Exp. Allergy* **50**, 189–197 (2020).
24. K. Asano *et al.*, A phase 2a study of DP2 antagonist GB001 for asthma. *J. Allergy Clin. Immunol. Pract.* **8**, 1275–1283.e1 (2020).
25. P. Santus, D. Radovanovic, Prostaglandin D2 receptor antagonists in early development as potential therapeutic options for asthma. *Expert Opin. Investig. Drugs* **25**, 1083–1092 (2016).
26. M. Calbet *et al.*, Pharmacological characterization of CRTh2 antagonist LAS191859: Long receptor residence time translates into long-lasting in vivo efficacy. *Pharmacol. Res.* **111**, 208–216 (2016).
27. L. Wang *et al.*, Structures of the human PGD_2 receptor CRTH2 reveal novel mechanisms for ligand recognition. *Mol. Cell* **72**, 48–59.e4 (2018).
28. M. Audet *et al.*, Crystal structure of misoprostol bound to the labor inducer prostaglandin E_2 receptor. *Nat. Chem. Biol.* **15**, 11–17 (2019). Correction in: *Nat. Chem. Biol.* **15**, 206 (2019).
29. H. Fan *et al.*, Structural basis for ligand recognition of the human thromboxane A_2 receptor. *Nat. Chem. Biol.* **15**, 27–33 (2019).
30. K. Morimoto *et al.*, Crystal structure of the endogenous agonist-bound prostanoid receptor EP3. *Nat. Chem. Biol.* **15**, 8–10 (2019).
31. Y. Toyoda *et al.*, Ligand binding to human prostaglandin E receptor EP_4 at the lipid-bilayer interface. *Nat. Chem. Biol.* **15**, 18–26 (2019).
32. S. Nojima *et al.*, Cryo-EM structure of the prostaglandin E receptor EP4 coupled to G protein. *Structure* **29**, 252–260.e6 (2021).
33. C. Qu *et al.*, Ligand recognition, unconventional activation, and G protein coupling of the prostaglandin E_2 receptor EP2 subtype. *Sci. Adv.* **7**, eabf1268 (2021).
34. G. Monneret, C. Cossette, S. Gravel, J. Rokach, W. S. Powell, 15R-methyl-prostaglandin D2 is a potent and selective CRTH2/DP2 receptor agonist in human eosinophils. *J. Pharmacol. Exp. Ther.* **304**, 349–355 (2003).
35. M. Caffrey, V. Cherezov, Crystallizing membrane proteins using lipidic mesophases. *Nat. Protoc.* **4**, 706–731 (2009).
36. D. M. Rosenbaum *et al.*, Structure and function of an irreversible agonist-β(2) adrenoceptor complex. *Nature* **469**, 236–240 (2011).
37. L. C. Johansson *et al.*, XFEL structures of the human MT_2 melatonin receptor reveal the basis of subtype selectivity. *Nature* **569**, 289–292 (2019).
38. B. Stauch *et al.*, Structural basis of ligand recognition at the human MT_1 melatonin receptor. *Nature* **569**, 284–288 (2019).
39. J. A. Ballesteros, H. Weinstein, Integrated methods for the construction of three-dimensional models and computational probing of structure-function relations in G protein-coupled receptors. *Method. Neurosci.* **25**, 366–428 (1995).
40. A. N. Hata, T. P. Lybrand, R. M. Breyer, Identification of determinants of ligand binding affinity and selectivity in the prostaglandin D2 receptor CRTH2. *J. Biol. Chem.* **280**, 32442–32451 (2005).
41. H. Sugimoto, M. Shichijo, M. Okano, K. B. Bacon, CRTH2-specific binding characteristics of [3H]ramatroban and its effects on PGD2-, 15-deoxy-Delta12, 14-PGJ2- and indomethacin-induced agonist responses. *Eur. J. Pharmacol.* **524**, 30–37 (2005).
42. N. Sawyer *et al.*, Molecular pharmacology of the human prostaglandin D2 receptor, CRTH2. *Br. J. Pharmacol.* **137**, 1163–1172 (2002).
43. X. Deupi, J. Standfuss, Structural insights into agonist-induced activation of G-protein-coupled receptors. *Curr. Opin. Struct. Biol.* **21**, 541–551 (2011).
44. B. Trzaskowski *et al.*, Action of molecular switches in GPCRs–Theoretical and experimental studies. *Curr. Med. Chem.* **19**, 1090–1109 (2012).
45. X. Prasanna, A. Chattopadhyay, D. Sengupta, "Role of Lipid-Mediated Effects in β2 - Adrenergic Receptor Dimerization" in *Biochemical Roles of Eukaryotic Cell Surface Macromolecules*, A. Chakrabarti, A. Surolia, Eds. (Springer, 2015), pp. 247–261.
46. S. M. Patra *et al.*, Differential dynamics of the serotonin1A receptor in membrane bilayers of varying cholesterol content revealed by all atom molecular dynamics simulation. *Mol. Membr. Biol.* **32**, 127–137 (2015).
47. X. Prasanna, D. Sengupta, A. Chattopadhyay, Cholesterol-dependent conformational plasticity in GPCR dimers. *Sci. Rep.* **6**, 31858 (2016).
48. D. S. Weber, J. J. Warren, The interaction between methionine and two aromatic amino acids is an abundant and multifunctional motif in proteins. *Arch. Biochem. Biophys.* **672**, 108053 (2019).
49. C. C. Valley *et al.*, The methionine-aromatic motif plays a unique role in stabilizing protein structure. *J. Biol. Chem.* **287**, 34979–34991 (2012).
50. E. A. Orabi, A. M. English, Modeling protein S–aromatic motifs reveals their structural and redox flexibility. *J. Phys. Chem. B* **122**, 3760–3770 (2018).
51. R. N. V. Krishna Deepak, B. Chandrakar, R. Sankararamakrishnan, Comparison of metal-binding strength between methionine and cysteine residues: Implications for the design of metal-binding motifs in proteins. *Biophys. Chem.* **224**, 32–39 (2017).
52. A. Gusach *et al.*, Structural basis of ligand selectivity and disease mutations in cysteinyl leukotriene receptors. *Nat. Commun.* **10**, 5573 (2019).
53. A. Luginina *et al.*, Structure-based mechanism of cysteinyl leukotriene receptor inhibition by antiasthmatic drugs. *Sci. Adv.* **5**, eaax2518 (2019).
54. Y. Zhuang *et al.*, Structure of formylpeptide receptor 2-G_i complex reveals insights into ligand recognition and signaling. *Nat. Commun.* **11**, 885 (2020).
55. T. Chen *et al.*, Structural basis of ligand binding modes at the human formyl peptide receptor 2. *Nat. Commun.* **11**, 1208 (2020).
56. Y. Lin, R. N. V. K. Deepak, J. Z. Zheng, H. Fan, L. Zheng, A dual substrate-accessing mechanism of a major facilitator superfamily protein facilitates lysophospholipid flipping across the cell membrane. *J. Biol. Chem.* **293**, 19919–19931 (2018).
57. W. Liu, A. Ishchenko, V. Cherezov, Preparation of microcrystals in lipidic cubic phase for serial femtosecond crystallography. *Nat. Protoc.* **9**, 2123–2134 (2014).
58. S. Boutet, G. J. Williams, The coherent X-ray imaging (CXI) instrument at the Linac Coherent Light Source (LCLS). *New J. Phys.* **12**, 035024 (2010).
59. A. Barty *et al.*, *Cheetah*: Software for high-throughput reduction and analysis of serial femtosecond X-ray diffraction data. *J. Appl. Cryst.* **47**, 1118–1131 (2014).
60. T. A. White *et al.*, Recent developments in *CrystFEL*. *J. Appl. Cryst.* **49**, 680–689 (2016).
61. I. J. Tickle *et al.*, STARANISO (Global Phasing Ltd., Cambridge, United Kingdom, 2018).
62. J. B. Klauda *et al.*, Update of the CHARMM all-atom additive force field for lipids: Validation on six lipid types. *J. Phys. Chem. B* **114**, 7830–7843 (2010).
63. K. Vanommeslaeghe *et al.*, CHARMM general force field: A force field for drug-like molecules compatible with the CHARMM all-atom additive biological force fields. *J. Comput. Chem.* **31**, 671–690 (2010).
64. K. Vanommeslaeghe, A. D. MacKerell Jr, Automation of the CHARMM General Force Field (CGenFF) I: Bond perception and atom typing. *J. Chem. Inf. Model.* **52**, 3144–3154 (2012).
65. K. Vanommeslaeghe, E. P. Raman, A. D. MacKerell Jr, Automation of the CHARMM General Force Field (CGenFF) II: Assignment of bonded parameters and partial atomic charges. *J. Chem. Inf. Model.* **52**, 3155–3168 (2012).
66. M. J. Abraham *et al.*, GROMACS: High performance molecular simulations through multi-level parallelism from laptops to supercomputers. *SoftwareX* **1**, 19–25 (2015).
67. B. Hess, H. Bekker, H. J. C. Berendsen, J. G. E. M. Fraaije, LINCS: A linear constraint solver for molecular simulations. *J. Comput. Chem.* **18**, 1463–1472 (1997).